HHS Public Access

Author manuscript

Shape Med Imaging (2018). Author manuscript; available in PMC 2019 April 17.

Published in final edited form as:

Shape Med Imaging (2018). 2018 September ; 11167: 28–37. doi:10.1007/978-3-030-04747-4_3.

Characterizing Anatomical Variability And Alzheimer's Disease Related Cortical Thinning in the Medial Temporal Lobe Using Graph-Based Groupwise Registration And Point Set Geodesic Shooting

Long Xie[1], **Laura E.M. Wisse**[1], **Sandhitsu R. Das**[1,3], **Ranjit Ittyerah**[1], **Jiancong Wang**[1], **David A. Wolk**[2,3], and **Paul A. Yushkevich**[1] **Alzheimer's Disease Neuroimaging Initiative**

[1]Penn Image Computing and Science Laboratory (PICSL), Department of Radiology, University of Pennsylvania, Philadelphia, USA

[2]Penn Memory Center, University of Pennsylvania, Philadelphia, USA

[3]Department of Neurology, University of Pennsylvania, Philadelphia, USA

Abstract

The perirhinal cortex (PRC) is a site of early neurofibrillary tangle (NFT) pathology in Alzheimer's disease (AD). Subtle morphological changes in the PRC have been reported in MRI studies of early AD, which has significance for clinical trials targeting preclinical AD. However, the PRC exhibits considerable anatomical variability with multiple *discrete variants* described in the neuroanatomy literature. We hypothesize that different anatomical variants are associated with different patterns of AD-related effects in the PRC. Single-template approaches conventionally used for automated image-based brain morphometry are ill-equipped to test this hypothesis. This study uses graph-based groupwise registration and diffeomorphic landmark matching with geodesic shooting to build statistical shape models of discrete PRC variants and examine variant-specific effects of AD on PRC shape and thickness. Experimental results demonstrate that the statistical models recover the folding patterns of the known PRC variants and capture the expected shape variability within the population. By applying the proposed pipeline to a large dataset with subjects from different stages in the AD spectrum, we find 1) a pattern of cortical thinning consistent with the NFT pathology progression, 2) different patterns of the initial spatial distribution of cortical thinning between anatomical variants, and 3) an effect of AD on medial temporal lobe shape. As such, the proposed pipeline could have important utility in the early detection and monitoring of AD.

1 Introduction

The human brain is highly variable in terms of its folding pattern and cytoarchitectural boundaries. Current leading paradigms in population studies using brain structural MRI are primarily based on normalization techniques that use a single template to capture variability between all subjects in a population, even when one to one correspondence between

anatomies might not exist. Failing to account for the anatomical variability in the analysis degrades our ability to reliably localize and accurately quantify brain regions in individual subjects. Although characterizing anatomical variability of the brain "on a whole" is desirable, it might not be feasible given an almost infinite number of anatomical configurations. However, when focusing on specific local brain regions, regional anatomical variability can often be described by a few anatomical variants. A recent study by Ding and Van Hoesen [1] found that in the human perirhinal cortex (PRC), two major anatomical variants account for 97% of the cases. The PRC, consisting of Brodmann areas 35 and 36 (BA35/36), plays an important role in memory and is a site of early neurofibrillary tangle (NFT) pathology, which is linked to synaptic loss and cell death in Alzheimer's disease (AD). The two variants are characterized by the morphology of the collateral sulcus (CS) (continuous vs. discontinuous CS). Given the early involvement of the PRC in AD, there is considerable interest in using MRI-based measures of its atrophy as biomarkers, e.g., for tracking the effectiveness of future drugs targeting NFT pathology in preclinical AD stages. However, it is important to ensure that such biomarkers take into account the anatomical variability of the PRC, since the extents of AD-related pathology in the PRC are likely to differ between the different anatomical variants due to the sheet-like organization of the cerebral cortex. For example, for subjects with deeper CS, early NFT deposition may occur more medially than for subjects with a shallow CS.

In our prior work [2], [3], we showed that graph-based multi-template analysis better accounts for the existence of discrete PRC variants and improves the quality of template fitting and sensitivity to AD effects. The current paper goes further to show that, by coupling with geodesic shooting for diffeomorphic shape matching [4], [5], the graph-based multi-template analysis is able to characterize PRC anatomical variability that is more meaningful than a conventional single-template approach. Furthermore, our paper compares patterns of AD-related change between PRC anatomical variants. Disambiguating these patterns using multi-template analysis may lead to more sensitive MRI-based measurements of early AD-related changes in the PRC, which may in turn provide more effective biomarkers for monitoring change in preclinical AD research and clinical trials.

2 Materials and Method

2.1 Dataset

This paper uses two MRI datasets. A publicly available dataset described in [6] (referred to as **T1-atlas**) with manual segmentations of BA35, BA36, entorhinal cortex (ERC), CS and meninges is used for multi-atlas segmentation and to define shape models of anatomical variants of the PRC. It consists of 29 [14 mild cognitive impairment (MCI), 15 normal control (NC)] 1.0 mm^3 MPRAGE T1-weighted MRI scans (T1w) upsampled to 0.5×0.5×1 mm^3 using a super-resolution technique [7] (SR-T1w).

Shape models derived from the T1-atlas are used to analyze a large dataset of baseline T1w MRIs from the Alzheimer's Disease Neuroimaging Initiative (ADNI). ADNI subjects (n = 603, see Table 1) were grouped into five severity categories based on diagnosis, cognitive symptoms and PET evidence of amyloid pathology: amyloid negative controls (AN-CN, n = 180) and amyloid positive controls, (AP-NC, n = 94), early MCI (AP-EMCI, n = 130), late

MCI (AP-LMCI, n = 109), and AD (AP-AD, n = 81). These categories reflect the continuum from cognitively normal to mild AD.

2.2 Construction of Statistical Models of Anatomical Variants of the PRC

To boost the size of the T1-atlas, images were flipped across the midsagittal plane, yielding a total of 58 samples. Manual segmentations were assigned by visual inspection to one of two variants (1: continuous CS vs. 2: discontinuous CS, [1]). Then, a statistical model for each variant was constructed using the following steps.

2.2.1 Template Construction Using Graph-Based Groupwise Registration—

A graph-based groupwise registration method similar to [8] is used to construct a population template of each anatomical variant (variant-template). First, we construct an undirected complete graph with the samples as vertices and edge weights indicative of dissimilarity between pairs of samples. To obtain the weights, affine and coarse-scale deformable diffeomorphic registration is performed between each pair of multi-label manual segmentations in the atlas. This uses a fast greedy diffeomorphic implementation adapted from [9], [10][b], with the sum of normalized cross correlation computed separately for each label as the image similarity metric. Importantly, a large spatial regularization term (the smoothing Gaussian kernel size is set to a 2.0 mm, which is a large value considering the PRC is a small structure) is applied during diffeomorphic registration to limit the amount of deformation that is allowed. Then, the weight of each pair of segmentations is measured as the one minus the generalized Dice similarity coefficient (GDSC) [11] of labels BA35, BA36 and CS between the warped moving segmentation and the segmentation of the target sample. Due to strong regularization, deformable registration can only correct for coarse-scale differences in shape, which makes the residual disagreement measured by one minus GDSC indicative of anatomical dissimilarity. Once the graph is generated, we construct a minimum spanning tree that includes all the nodes in the graph [12] and mark as its “root” the sample that has the shortest path along the tree to all the nodes. The shortest path from each sample to the MST root corresponds to a sequence of affine and deformable registrations that involves the least amount of deformation at each step. A unique path from each sample to the root is then identified. For each sample, a second set of finer-scale deformable registrations (with the smoothing kernel size set to 0.8 mm) are performed between each pair of samples along the unique path. Then, we compose the sequence of affine transforms and finer-scale deformations (rather than the coarse deformations) along these unique paths and warp the segmentations of all the samples to the space of the root sample. In order to further align all the samples, at the end of this step, a population template is built from the warped multi-label segmentations in the space of the root sample using the same metric as in the pairwise coarse registration by applying the iterative unbiased template building algorithm [9].

2.2.2 Quantifying Shape Variability Using Pointset Geodesic Shooting—

Subsequent shape analysis uses a large deformation diffeomorphic metric mapping (LDDMM) on point landmarks via geodesic shooting [4], [5], [13]. This provides several

[b]“Greedy” tool (https://github.com/pyushkevich/greedy)

benefits: (1) diffeomorphic transformations of the template shape toward each of the subject shapes can be represented compactly using the initial momentum vector field; (2) linear statistics such as PCA can be applied to the initial momenta to characterize variability and to generate statistically plausible shapes; (3) landmark matching is simpler and more efficient than image-based geodesic shooting, and makes particular sense for matching multi-label images; (4) landmark correspondences can be easily interpolated to yield diffeomorphic transformations of the entire image domain. Using geodesic shooting in Section 2.2.1 will make the pipeline more consistent. However, performing N^2 registrations in the pairwise registration step using geodesic shooting is not efficient and impractical. Since we aim to develop an efficient pipeline for our application, we choose to use a fast implementation of the greedy registration approach instead.

For each variant-template, we first generate a dense surface mesh (M^T, 10^4 vertices) for the union of ERC, BA35 and BA36 labels, on which we uniformly sample a sparse set of L point landmarks $X^T = \{X_1^T, \ldots, X_L^T\}$ (about 2500 landmarks are sampled.) using Poisson Disk Sampling [14]. The landmarks are then warped to the space of each sample i of the N samples using the deformation field generated in Section 2.2.1, denoted as $X_i = \{X_{i,1}, \ldots, X_{i,L}\}$. The Procrustes algorithm [15] is applied to rigidly align X_I to X^T, denoted as $\hat{X}_i$. Then geodesic shooting is performed between $\hat{X}_i$ and X^T to generate the initial momenta of all the subjects. We follow the notation of the geodesic shooting method in [4]. Let α be a $L \times 3$ matrix of the landmarks' initial momenta. Let $q(t; \alpha) = \{q_1(t; \alpha), \ldots, q_L(t; \alpha)\}$ describe the evolution of landmark positions over time $t \in [0,1]$and let $p(t; \alpha) = \{p_1(t; \alpha), \ldots, p_L(t; \alpha)\}$ be the corresponding evolving momenta at time point t, with $q(0; \alpha) = X^T$, $p(0; \alpha) = \alpha$. The Hamiltonian $H(p,q) = \sum_j \sum_k e^{-|q_j - q_k|^2 / 2\sigma^2} p_j^T p_k$ describes the kinetic energy of the evolving landmark system and is constant over time; evolution is given by the system of equations $\left\{\frac{dq}{dt} = \frac{\partial H(q,p)}{\partial p}, \frac{dp}{dt} = -\frac{\partial H(q,p)}{\partial q}\right\}$ [16]. With this notation, the landmark-matching process can be formulated as an optimization problem for each sample i

$$\alpha_i^* = \arg \min_{\alpha \in \mathbb{R}^{3L}} H(X^T, \alpha) + \lambda \cdot \|q(1;\alpha) - \hat{X}_i\| \quad (1)$$

where λ is the weight of the fidelity term. The optimization problem is solved using a gradient-descent method as described in [4]. After optimization, a smooth time-varying velocity field over the entire spatial domain can be obtained from the optimal landmark trajectories $q(t; \alpha_i^*)$ and the corresponding momenta $p(t; \alpha_i^*)$ using *eqn* 2 and the diffeomorphic transformation over the image domain $\phi_I(x, t)$ can be derived by integrating the corresponding time points of the velocity field.

$$\frac{d\phi_i(x,t)}{dt} = v_i(x,t) = \sum_{l=1}^{L} G_\sigma(\|q_l(t;\alpha_i^*) - x\|) \cdot p_l(t;\alpha_i^*), x \epsilon \mathbb{R}^3 \quad (2)$$

A drawback of the graph-based groupwise registration approach (Sec 2.2.1) is that the template is very similar in shape to the root sample and may not be a good representation of the groupwise mean. We use an iterative approach to perform shape correction. Let $X^{T,0}$ be the landmark locations in the root template. At iteration k, we perform the following steps: (1) for each sample i, we rigidly align X_i to $X^{T,k}$ to generate $\hat{X}_i^k$, and α_i^k is obtained by geodesic shooting from $X^{T,k}$ to $\hat{X}_i^k$ (*eqn* 1), (2) we compute the average initial momentum $\bar{\alpha}^k = \frac{1}{N}\sum_{i=1}^{N} \alpha_i^k$, (3) the template landmarks $X^{T,k}$ are deformed by geodesic shooting in the direction of $\bar{\alpha}^k$ to generate $\hat{X}^{T,k+1}$, (4) to avoid expansion or shrinkage of the landmark configurations due to global scaling, $X^{T,k}$ are rigidly aligned to $\hat{X}^{T,k+1}$ to generate the updated template landmarks positions $X^{T,k+1}$ and the template surface mesh $M^{T,k}$ is updated to $M^{T,k+1}$ using the same rigid transformation. This process is repeated until the template becomes stable yielding the final template landmarks $X^{T,K}$ and the final template surface mesh $M^{T,K}$.

PCA is applied to the initial velocity fields, computed from the corresponding initial momenta generated in the last iteration, to quantify anatomical variability. Principal modes are visualized by applying geodesic shooting to $M^{T,K}$ along the principal eigenvectors in both the positive and negative directions.

2.3 Fitting the Templates to A New Target Image

(1) Automatic segmentation and template assignment.—A multi-atlas segmentation method [17] is used to generate automatic segmentations of bilateral MTL substructures in ADNI T1w MRI scans, using the T1-atlas as the atlas set. For a given target T1w MRI scan, let S_{tg} denote its segmentation. To automatically determine the anatomical variant of S_{tg}, similar to the pairwise registration step in Section 2.2.1, S_{tg} is coarsely registered to all the 58 samples in the T1-atlas and the GDSCs of labels BA35, BA36 and CS are computed. The six samples with the highest GDSCs are used to perform weighted (by GDSC) voting and the variant that gets the highest vote is assigned to the target sample.

(2) Template fitting.—The sample in the atlas set that belongs to the same anatomical variant with S_{tg} and yields the highest GDSC is identified, referred to as S_{bdg}. Then, the landmarks in the corresponding variant-template space, i.e. $X^{T,K}$, are warped to the space of the target sample, referred to as X_{tg}, using the deformation field generated by composing the deformations from the variant-template to S_{bdg} (obtained in Section 2.2.1) and from S_{bdg} to S_{tg} [generated in step (1) above]. Similar to that in Section 2.2.2, we (1) rigidly align X_{tg} to $X^{T,K}$ using Procrustes algorithm [15] to generate $\hat{X}_{tg}$, (2) compute the optimal α_{tg} by matching $X^{T,K}$ to $\hat{X}_{tg}$ and (3) deform $M^{T,K}$ to the space of each subject by applying the velocity field derived from α_{tg} using *eqn* 2.

3 Experiments and Results

3.1 Statistical Shape Models

In the T1-atlas, 24 cases were assigned to variant 1 and 34 samples to variant 2. Figure 1 shows the smooth variant-template meshes (first two rows, middle column) and the principal mode of variations of the two statistical models (Supplementary Videos S1). As expected, the two variant-templates resemble anatomical variants with continuous and discontinuous CS, respectively, and appear to be consistent with the anatomical subtypes described in [1]. The first PCA mode of variant 2 captures variation in the relative length of anterior and posterior CS. This variability makes anatomical sense, as variant 2 has been further dichotomized in anatomy literature into two subtypes based on the relative length of anterior and posterior CS [1]. This shows that the graph-based template-building approach is able to align subjects with discontinuous CS. The first PCA mode of variant 1 captures variation in the depth of the CS, which is also a recognized source of variability in this region [1].

To compare our multi-template pipeline with the conventional approach, we also build a statistical shape model for all the samples without grouping by anatomical variants (the third row in Figure 1, Supplementary Video S2). This single-template approach has two major limitations: (1) An anatomically implausible shape is observed in the middle of the CS (white arrow in Figure 1); (2) The first PCA mode appears to be less meaningful anatomically, capturing a combination of variability in depth of the CS and the relative length of anterior and posterior CS.

3.2 AD-Related Cortical Thinning

In the ADNI dataset, the number of subjects assigned to different anatomical variants by group is shown in Figure 2. Across all groups and both hemispheres, 558 (46%) samples were classified into variant 1 and 648 (54%) into variant 2. The proportion of variants between left and right is not significantly different ($\chi^2 = 2.6$, $p > 0.1$).

To evaluate the patterns of cortical thinning, regional thickness analyses were performed between the control group (AN-CN) and the 4 patient groups separately. Regional thickness is measured by first extracting the pruned Voronoi skeleton [18] of the fitted template mesh and computing the distance between each vertex and the closest point on the skeleton. A general linear model is fit at each vertex with thickness as the dependent variable, group membership as the factor of interest, and age, education as covariates. To account for multiple statistical comparisons, cluster-level familywise error rate correction is used [19] (empirical threshold: uncorrected $p = 0.05$). Permutation testing with 1000 iterations is used to assign a corrected p-value to each cluster. Analysis is performed separately for each variant of each hemisphere.

As shown in Figure 2, we observed a consistent pattern of disease progression across variant-templates of both hemispheres: initiating largely in BA35 as early as in the AP-EMCI stage and progressing to ERC and BA36 in later stages. This is consistent with neuropathological staging of NFT progression [20]. Cluster size, spatial distribution, and magnitude of significance increase along with disease severity. Also, significant clusters at later stages almost always cover the ones in the corresponding previous stages. No

significant effects are observed in AP-CN. Being able to replicate the patterns of disease progression in the MTL observed in *ex vivo* pathology studies using *in vivo* MRI (Figure 2) has great potential significance for tracking the early neurodegenerative stages of disease critical for measurement of intervention effects in clinical trials.

A novel aspect in this study is that we examine the relationship between the spread of AD-related atrophy and PRC variants. The first site of cortical thinning in variant 1 appears to be located at the fundus of the CS (gray arrows in Figure 2), whereas in variant 2, it is located more medially, at the boundary of ERC and BA35 (yellow arrows in Figure 2). There is not much difference between anatomical variants in later stages, probably because the majority of the MTL cortex is affected by the disease.

3.3 Effect of AD on MTL Shape

To investigate the effect of AD on MTL shape, for each variant, the initial momenta of subjects from the opposite ends of the AD spectrum, i.e. AN-CN and AP-AD (excluded cases from the other groups), are converted to initial velocity fields and projected to the first m PCA modes that account for 95% of the total variance of the corresponding statistical model (m = 19/26 for variant 1/2 respectively) and a support vector machine (SVM) with a linear kernel [21] is trained on the PCA loadings to discriminate the two groups. The vector orthogonal to the SVM hyperplane, which is assumed to be the direction that best discriminates the two groups, is shown in Figure 3 (Supplementary Videos S3). The result shows that AD is associated with decrease in overall size of the MTL, cortical thinning and widening of the CS. It will be interesting to investigate in future studies whether these shape features provide complementary information in identifying disease groups.

4 Conclusion

In this study, we propose a novel analysis pipeline to quantify shape variability of anatomical variants of the PRC. Experimental results demonstrate that the statistical models recover the folding patterns of the known anatomical variants of the PRC defined in the neuroanatomy literature and capture the expected shape variability within the population. In addition, when applied to a large dataset with subjects from different stages in the AD spectrum, the novel shape analysis reveals a progression of cortical thinning and shape that is consistent with known progression of NFT pathology within the MTL cortex related to AD. Also, different patterns of the spatial distribution of cortical thinning are observed between anatomical variants. Summary thickness measurements extracted from the significant clusters (Figure 2) and the features associated with shape changes may be useful markers for early detection and tracking disease progression. As such, we believe the proposed method may have important utility in the early detection and monitoring of AD and the findings in this study may help us better understand the effect of AD on the shape of MTL substructures.

Supplementary Material

Refer to Web version on PubMed Central for supplementary material.

Acknowledgements.

This work was supported by NIH (grant numbers R01-AG056014, R01-AG040271, P30-AG010124, R01-EB017255, AG055005) and the donors of Alzheimer's Disease Research, a program of the BrightFocus Foundation (L.E.M.W.).

References

[1]. Ding S-L and Van Hoesen GW, "Borders, extent, and topography of human perirhinal cortex as revealed using multiple modern neuroanatomical and pathological markers.," Hum. Brain Mapp, vol. 31, no. 9, pp. 1359–79, 9 2010. [PubMed: 20082329]

[2]. Xie L, Pluta J, Wang H, Das SR, Mancuso L, Kliot D, Avants BB, Ding S-L, Wolk DA, and Yushkevich PA, "Automatic clustering and thickness measurement of anatomical variants of the human perirhinal cortex," in Medical Image Computing and Computer-Assisted Intervention-MICCAI 2014, 2014, pp. 81–88.

[3]. Xie L, Pluta JB, Das SR, Wisse LEM, Wang H, Mancuso L, Kliot D, Avants BB, Ding S-L, Manjón JV, Wolk DA, and Yushkevich PA, "Multi-template analysis of human perirhinal cortex in brain MRI: Explicitly accounting for anatomical variability," Neuroimage, vol. 144, pp. 183–202, 2017. [PubMed: 27702610]

[4]. Allassonniere S, Trouve A, and Younes L, "Geodesic shooting and diffeomorphic matching via textured meshes," EMMCVPR '05 Proc. 5th Int. Work. Energ. Minim. Meth. Comput. Vis. PatternRecogn., pp. 365–381, 2005.

[5]. Vaillant M, Miller MI, Younes L, and Trouvé A, "Statistics on diffeomorphisms via tangent space representations.," Neuroimage, vol. 23 Suppl 1, pp. S161–9, 1 2004. [PubMed: 15501085]

[6]. Xie L, Wisse LEM, Das SR, Wang H, Wolk DA, Manjón JV, and Yushkevich PA, "Accounting for the Confound of Meninges in Segmenting Entorhinal and Perirhinal Cortices in T1-Weighted MRI," in Medical Image Computing and Computer-Assisted Intervention-MICCAI 2016, 2016, pp. 564–571.

[7]. V Manjón J, Coupé P, Buades A, Fonov V, Collins LD, and Robles M, "Non-local MRI upsampling.," Med. Image Anal, vol. 14, no. 6, pp. 784–92, 12 2010. [PubMed: 20566298]

[8]. Wu G, Jia H, Wang Q, and Shen D, "SharpMean: groupwise registration guided by sharp mean image and tree-based registration.," Neuroimage, vol. 56, no. 4, pp. 1968–81, 6 2011. [PubMed: 21440646]

[9]. Joshi S, Davis B, Jomier M, and Gerig G, "Unbiased diffeomorphic atlas construction for computational anatomy.," Neuroimage, vol. 23 Suppl 1, pp. S151–60, 1 2004. [PubMed: 15501084]

[10]. Avants BB, Epstein CL, Grossman M, and Gee JC, "Symmetric diffeomorphic image registration with cross-correlation: evaluating automated labeling of elderly and neurodegenerative brain.," Med. Image Anal, vol. 12, no. 1, pp. 26–41, 2 2008. [PubMed: 17659998]

[11]. Crum WR, Camara O, and Hill DLG, "Generalized overlap measures for evaluation and validation in medical image analysis.," IEEE Trans. Med. Imaging, vol. 25, no. 11, pp. 1451–61, 11 2006. [PubMed: 17117774]

[12]. Prim RC, "Shortest connection networks and some generalizations," Bell Syst. Tech. J, vol. 36, no. 6, pp. 1389–1401, 11 1957.

[13]. Miller MI, Trouvé A, and Younes L, "Geodesic Shooting for Computational Anatomy.," J. Math. Imaging Vis, vol. 24, no. 2, pp. 209–228, 1 2006. [PubMed: 20613972]

[14]. Corsini M, Cignoni P, and Scopigno R, "Efficient and Flexible Sampling with Blue Noise Properties of Triangular Meshes," IEEE Trans. Vis. Comput. Graph, vol. 18, no. 6, pp. 914–924, 6 2012. [PubMed: 22291147]

[15]. Dryden IL and V Mardia K, Statistical Shape Analysis, with Applications in {R}. Second Edition. Chichester: John Wiley and Sons, 2016.

[16]. Ott E, Chaos in dynamical systems. Cambridge University Press, 2002.

[17]. Yushkevich PA, Pluta JB, Wang H, Xie L, Ding S, Gertje EC, Mancuso L, Kliot D, Das SR, and Wolk DA, "Automated volumetry and regional thickness analysis of hippocampal subfields and

medial temporal cortical structures in mild cognitive impairment," Hum. Brain Mapp, vol. 36, no. 1, pp. 258–287, 2015. [PubMed: 25181316]

[18]. Ogniewicz RL and Kübler O, "Hierarchic Voronoi skeletons," Pattern Recognit, vol. 28, no. 3, pp. 343–359, 3 1995.

[19]. Nichols T and Hayasaka S, "Controlling the familywise error rate in functional neuroimaging: a comparative review.," Stat. Methods Med. Res, vol. 12, no. 5, pp. 419–46, 10 2003. [PubMed: 14599004]

[20]. Braak H and Braak E, "Staging of Alzheimer's disease-related neurofibrillary changes," Neurobiol. Aging, vol. 16, no. 3, pp. 271–278, 1995. [PubMed: 7566337]

[21]. Vapnik VN, Statistical learning theory. Wiley, 1998.

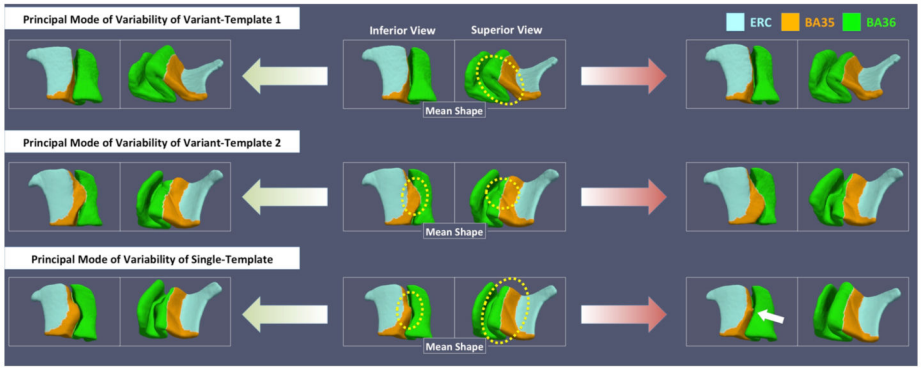

Figure 1.

The variant-templates (the first and second rows) and single-template (the third row), and their corresponding principal modes of variability. Yellow dashed circles highlight the regions with the most variability. White arrow indicates the anatomically implausible structure in the single-template. Videos are available in Supplementary Videos S1 (variant templates 1 and 2) and S2 (single template).

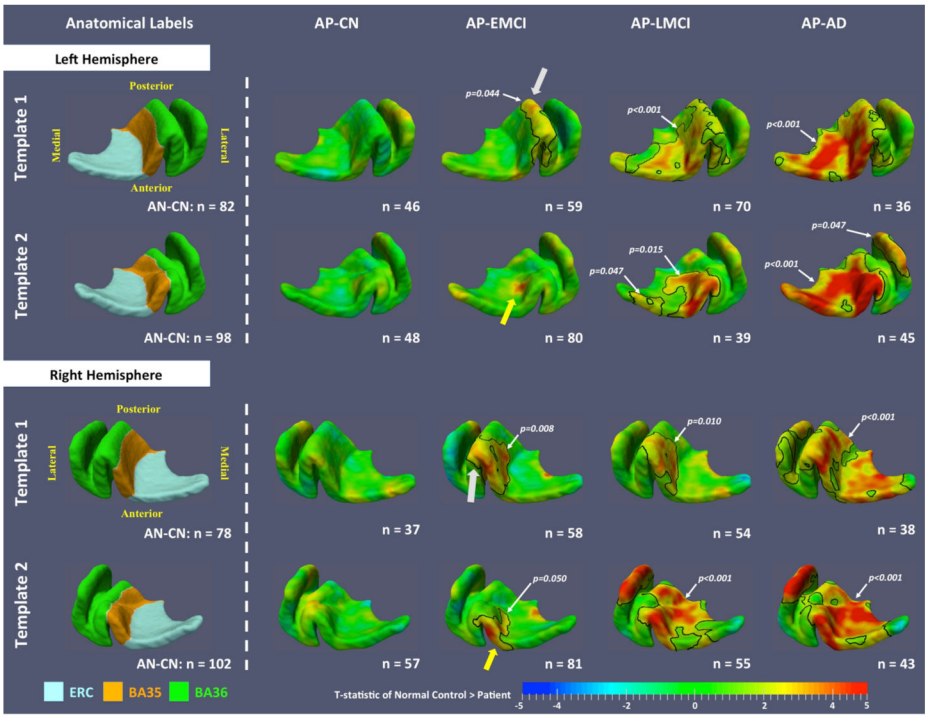

Figure 2.

t-statistical maps of the contrast between AN-CN and four disease groups. Black contours outline significant clusters and the corrected p-values are indicated by the white arrow and text. The corresponding anatomical labels are shown in the first column.

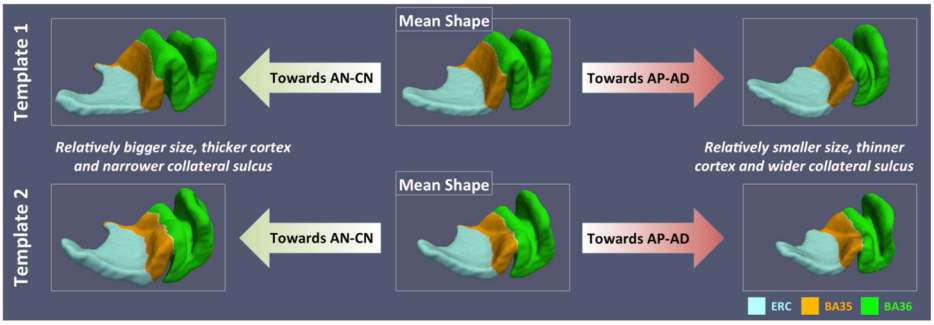

Figure 3.

The effect of AD on medial temporal lobe cortex shape of the anatomical variants. Videos are available in Supplementary Videos S3.

Table 1.

Demographics of the ADNI dataset

	AN-CN	AP-CN	AP-EMCI	AP-LMCI	AP-AD
N	180	94	130	109	81
Age (yrs.)	72.0 (6.0)	74.5 (5.7) ***	73.0 (6.9)	71.7 (6.8)	74.9 (7.8) ***
Gender (M/F)	94 / 86	32 / 62 **	80 / 59	57 / 52	47 / 34
Education (yrs.)	16.9 (2.4)	16.1 (2.7) *	15.7 (2.9) ***	16.6 (2.6)	15.4 (2.6) **
MMSE	29.0 (1.3)	29.0 (1.1)	28.0 (1.7) ***	27.2 (1.9) ***	23.2 (2.1) ***

Note: All statistics are in comparison to AN-CN. Two-sample t-test (age, education and MMSE) and χ^2 test (gender) are used.

* $p < 0.05$

** $p < 0.01$

*** $p < 0.001$. MMSE = mini-mental state examination.